Research Square

Preprints are preliminary reports that have not undergone peer review.
They should not be considered conclusive, used to inform clinical practice,
or referenced by the media as validated information.

Discrete element study on indentation delamination failure and mechanical properties of thermal barrier coatings with random pore defects

Hongfei Gao

tgghf1112@163.com

Chifeng Industry Vocational Technology College

Minglei Bai

Chifeng Industry Vocational Technology College

Article

Keywords: Random pore defects, Discrete Element model, Thermal barrier coatings

Posted Date: November 6th, 2026

DOI: https://doi.org/10.21203/rs.3.rs-11349524/v1

License: This work is licensed under a Creative Commons Attribution 4.0 International License.
Read Full License

Additional Declarations: No competing interests reported.

Abstract

Indentation damage is a typical failure mode of thermal barrier coatings (TBCs). In this study, A discrete element method (DEM)model of TBCs with random pore defects was developed to study the effects of pore density and pore shape on delamination cracking and mechanical properties under indentation loading. The results indicate that as pore density increases, the length of interfacial delamination cracks decreases, suggesting that pores can impede crack propagation. Accordingly, a pore density factor was defined to quantitatively characterize this negative correlation. Regarding the influence of pore shape on coating damage, Sharp corners are prone to inducing stress concentration, thereby accelerating crack initiation and propagation. With increasing pore density, the indentation modulus and hardness of the coating decrease. The simulation results show good agreement with Mori–Tanaka (M–T) theoretical predictions and existing experimental data. This study provides a theoretical basis for pore control, indentation failure assessment, and life prediction of thermal barrier coatings.

1. Introduction

Thermal barrier coatings (TBCs) are primarily applied to critical components in aerospace high-temperature fields, such as gas turbine engines and blades. It can provide thermal insulation protection for coated components, reduce their operating temperature, and prevent the coated materials from wear during long-term service[1–3]. However, during the preparation of TBCs, pore defects are inevitably introduced into the coating interior due to factors such as inappropriate spraying process parameters and non-compliant deposition environments. When subjected to external loads such as tension, compression, or impact, the presence of these pore defects can severely degrade the mechanical properties of the coating material[4, 5].

Previous studies have mainly focused on the relationship between interface irregularity and interfacial crack propagation[6, 7], whereas the influence of microscopic pore defects on crack propagation within the coating has not been clearly elucidated. In fact, since the sizes of pores within TBCs generally range from the micrometer to the nanometer scale, the size, shape, and other characteristics of micropore defects are difficult to control precisely during preparation, making it impossible to capture the crack propagation behavior in real materials at the experimental level[8]. Although some theoretical studies have provided qualitative explanations for the crack formation process, most of them neglect the geometric diversity of micropores and are unable to quantitatively characterize the influence of pore characteristics on the stress field redistribution and crack propagation path within the coating[9, 10]. Therefore, it is necessary to develop a research approach that can overcome the limitations of traditional experiments and conventional theoretical analysis, so as to precisely and controllably investigate the intrinsic correlation between the geometric parameters of micropore defects and the mechanical damage characteristics of TBCs.

In recent years, numerical simulation techniques have gradually become an important means for studying the microscopic damage mechanisms of materials, owing to their outstanding advantages of

high precision, reproducibility, and microscopic visualization. For example, the finite element method (FEM)[11]、boundary element method (BEM)[12] and the discrete element method (DEM)[13] can accurately reconstruct the microscopic structure of TBCs containing realistic micropore defects, enabling independent and quantitative control of parameters. However, the FEM is complex to implement, computationally intensive, and prone to non-convergence when establishing a large number of pores[14]. In contrast, the DEM avoids these problems and offers significant advantages in microscopic defect evolution and discrete damage characterization, providing reliable technical support for quantitatively revealing the crack propagation mechanisms of TBCs under different pore characteristics.

This paper aims to overcome the limitations of traditional experimental characterization in the study of micropore defects. A DEM model of a TBCs system containing random pore defects is established. The damage evolution law of TBCs containing random pore defects under indentation loading is revealed. A quantitative relationship between random pore characteristics and delamination crack length is established. The crack propagation mechanism within the coating system is elucidated from a microscopic perspective. This study provides a theoretical reference for pore

defect control during the spraying preparation of TBCs, indentation failure assessment, and service life prediction of coatings.

2. Description of the DEM

2.1 Principle of the DEM

The DEM was first proposed by Cundall and Strack[15] in 1979 based on molecular dynamics, and was initially applied to the analysis of rock mechanics. After years of development, this method has demonstrated great potential in analyzing the damage, fracture, and post-fracture behavior of brittle materials.

The computational principle of the DEM is to divide the research object into a finite number of particles. As shown in Fig. 1a., particles can contact and overlap with each other, which generates contact forces between particles. As shown in Fig. 1b, According to Newton's second law and the force–displacement law, the translational and rotational equations are given in Eqs. (1) and (2), respectively:

Translation: (1)

Rotation: (2)

Where m_i、x_i、θ_i、I_i represent the mass, displacement, rotation angle, and moment of inertia of the *i*-th particle, respectively, is the gravitational acceleration, *t* is the time, $N_p$represents the total number of particles in contact with particle *i*, F_{ij} and M_{ij}represent the contact force and moment exerted by particle *j* on particle *i*, respectively.

In the DEM, several built-in models are available for simulating bonded contacts between particles, including the contact bond model and the linear parallel bond model. Among them, the contact bond model can only transmit forces, whereas the parallel bond model can transmit both forces and bending moments. The latter is therefore more suitable for simulating brittle materials such as rocks and ceramics. Consequently, the parallel bond model was selected as the contact model for the ceramic layer in this study. The contact force and contact moment of the linear parallel bond model follow the laws given below:

$$F_c = F^l + F^d + \overline{F} \quad (3)$$

$$M_c = \overline{M} \quad (4)$$

Where $F^l$is the linear force, $F^d$is the damping force, $\overline{F}$ is the parallel bond force, and $\overline{M}$ is the parallel bond moment.

2.2 Parameter calibration of DEM

The software used in this study is PFC2D (Particle Flow Code 2D). It is specifically designed for simulating and analyzing the behavior of particle systems, and has been applied in various fields such as mining, geotechnical engineering, architecture, and materials science. PFC simulates the interactions between microscopic particles within materials using a particle-based approach., making it particularly suitable for studying materials exhibiting discrete and discontinuous behavior, such as brittle solids.

In the DEM, the mechanical properties of materials usually need to be calibrated through virtual microscopic unit tests. Therefore, commonly used microscopic unit tests were adopted in this study, as shown in Fig. 2, which correspond to the uniaxial compression test, three-point bending test, and fracture toughness test, respectively.

Through uniaxial compression test on the model, the elastic modulus *E*, Poisson's ratio , and compressive strength σ_c of the material can be obtained. Previous studies have shown that in uniaxial compression tests, when the ratio of the specimen height to width is 2, the overall stress distribution within the model is relatively uniform[16]. As shown in Fig. 2a, the dimensions of the uniaxial compression model are 19.2 × 38.4 μm. In numerical simulation, this can be simplified as two walls moving toward each other to compress the material. Zhang[17] pointed out that the acceptable upper limit of the loading velocity is 0.08 m/s. To ensure static loading, the wall velocity was set to 0.05 m/s in this study until the specimen failed. The compressive strength σ_c is the peak stress in the compression test, which can be directly obtained from the curve, while the elastic modulus and Poisson's ratio can be calculated using Eqs. (5) and (6)

$$E = \frac{(\sigma_2 - \sigma_1)}{(\varepsilon_{A2} - \varepsilon_{A1})} \quad (5)$$

$$v = \frac{(\varepsilon_{T2} - \varepsilon_{T1})}{(\varepsilon_{A2} - \varepsilon_{A1})} \quad (6)$$

Where σ_1 and σ_2 are the axial stresses corresponding to the linear stage, ε_{A1} and ε_{A2} are the corresponding axial strains, ε_{T1} and ε_{T2} are the corresponding lateral strains.

As shown in Fig. 2b, the three-point bending test can be used to obtain the flexural strength of the material. The dimensions of the three-point bending specimen are 61.762 × 11.2 μm, with a span of 44.8 μm. The upper circular indenter moves downward at a velocity of 0.02 m/s until the specimen fractures at the central axis. The flexural strength is calculated using Eq. (7):

$$\sigma_b = \frac{3F_{\max 1}l}{2bh^2} \quad (7)$$

Where $F_{\max 1}$ is the maximum load borne by the upper circular indenter, *l* is the distance between the two lower supports, *b* is the thickness of the specimen (taken as 1 in the two-dimensional case), and *h* is the height of the specimen.

As shown in Fig. 2c, the fracture toughness test was conducted. In this test, a notch was created by deleting particles at the center near the bottom of the specimen, with a notch depth of 5.6 μm and a width of 0.227 μm. The upper circular indenter moved downward at a velocity of 0.02 m/s until the specimen completely fractured. The fracture toughness is calculated using Eqs. (8) and (9):

$$K_{IC} = \frac{F_{\max 2}l}{bw^{\frac{3}{2}}} f_1\left(\frac{a}{w}\right) \quad (8)$$

$$f_1\left(\frac{a}{w}\right) = 2.9\left(\frac{a}{w}\right)^{\frac{1}{2}} - 4.6\left(\frac{a}{w}\right)^{\frac{3}{2}} + 21.8\left(\frac{a}{w}\right)^{\frac{5}{2}} - 37.6\left(\frac{a}{w}\right)^{\frac{7}{2}} + 38.7\left(\frac{a}{w}\right)^{\frac{9}{2}} \quad (9)$$

Where $F_{\max 2}$ is the maximum load borne by the indenter, *l* is the distance between the two lower supports, *b* is the thickness of the specimen (taken as 1 in the two-dimensional case), *w* is the height of the specimen, and *a* is the notch depth.

According to the microscopic unit tests and the calculations based on Eqs. (5)-(9), the mechanical property parameters of the ceramic layer, bond coat, and substrate in the thermal barrier coating were finally obtained, as listed in Table 1:

Table 1
Mechanical properties of ceramic coat, bond coat and substrate

Mechanical property		Simulation values (this work)	Experiment values[18–20]	Relative error
Ceramic coat	Poisson's ratio ν	0.263	0.28	6.07%
	Elastic modulus (GPa)	271.79	270	0.66%
	Bending strength σ_b(MPa)	72.91	76.5	4.69%
	Compressive strength σ_c(MPa)	208.72	227	8.05%
	Fracture toughnessK_{IC} (MPa·m$^{1/2}$)	2.24	2.05	9.27%
Bond coat	Elastic modulus (GPa)	186	183	1.639%
	Poisson's ratio ν	0.29	0.3	3.300%
	Tensile strength σ_t(MPa)	420	416	0.961%
Substrate	Elastic modulus (GPa)	182	187	2.673%
	Poisson's ratio ν	0.31	0.3	3.333%
	Tensile strength σ_t(MPa)	1139	1150	0.957%
	Shear strength σ_s(MPa)	803	780	2.949%

As can be seen from Table 1, the errors between the simulated and experimental values of the mechanical properties are all below 10%, indicating that the calibration results for the mechanical properties of the ceramic layer, bond coat, and substrate meet the requirements. Therefore, this set of parameters can be used as the mechanical parameters of the numerical model.

3. Discrete element modeling of TBCs under indentation loading

As shown in Fig. 3, the microscopic SEM image of the EB-PVD coating reveals that random pore defects of various shapes and sizes are distributed within the ceramic layer. Since the ceramic layer itself is a brittle material lacking the capacity for plastic deformation, it is highly prone to cracking under indentation or impact loading. Therefore, reasonable control of pores can, to a certain extent, alleviate

stress concentration, disperse external stresses, and enhance the damage resistance of the coating. Accordingly, this section establishes a discrete element model of TBCs containing random pore defects, aiming to explore the influence of random pore defect distribution on TBCs damage under indentation loading, and reveal the crack propagation mechanism within the coating system from a microscopic perspective.

The structure of the TBCs system is shown in Fig. 4a. The system consists of a ceramic top coat (TC), a metallic bond coat (BC), and a metallic substrate (Sub). Random circular pores, with a radius denoted as *r*, are distributed within the TC layer.

As shown in Fig. 4b, when an indentation load is applied to the surface of the thermal barrier coating, the TC layer is locally subjected to high compressive and shear stresses, resulting in the formation of shear bands. At the interface between the TC layer and the BC layer, delamination cracks form due to tensile stress. These delamination cracks continue to extend along the interface as the load increases, further weakening the coating and eventually leading to large-area spalling of the coating.

The discrete element model of the TBCs system is shown in Fig. 4c. The total length of the model is 2000 μm; the heights of the TC layer and the Sub layer are both 200 μm, and the height of the BC layer is 50 μm, which conforms to the standard dimensions of an actual coating system. The circular pores are implemented in the model by deleting particles. The indenter is represented by a wall in the PFC software. The indenter is assumed to be rigid and has the shape of a Vickers indenter (with a bottom angle of 136°), moving downward at a velocity of 0.01 m/s.

The results show that when the penetration depth of the indenter reaches 100 μm, cracks propagate downward from the surface of the TC layer and penetrate through the TC layer along the grain boundaries, eventually extending to the TC/BC interface. During this process, a large number of tensile cracks concentrate beneath the indenter, and the TC layer material in the region below the indenter undergoes damage. The cracks continue to propagate laterally along the interface direction, causing the TC layer and the BC layer to completely separate and spall. Meanwhile, influenced by local stress concentration and shear stress, shear bands form within the TC layer. The numerical simulation results are consistent with the experimental results, thereby validating the effectiveness of the numerical model.

4. Results and discussion

4.1 Effect of pore density on delamination cracks

In the two-dimensional model, the pore density is expressed as the ratio of the total pore area to the total model area[23], denoted by *d*. The pore density within the TC layer typically ranges from 0.04 to 0.2[24]. This section focuses on analyzing the influence of pore density, only circular pores are considered (the influence of pore shape will be discussed in Section 4.2), and the pore density is controlled by fixing the pore radius at 2 μm and adjusting the number of pores (ranging from 20 to 60 with an interval of 10), with $d = 0$ added as a control group.

Figure 5 shows the effect of different pore densities on the delamination crack propagation length under indentation loading. The overall trend indicates that the delamination crack length gradually decreases as the pore density increases. When *d* = 0, the delamination damage at the TC/BC interface is the most severe, with the single-side delamination crack length reaching 978.48 μm, and the TC layer and BC layer are almost completely separated. This indicates that in a dense structure, cracks tend to propagate along the interface and connect to form longer delamination cracks. When *d* = 0.0628, the delamination crack length is 907.91 μm, which is 7.21% shorter than that of the non-porous case, indicating that pore defects impede crack propagation. Pores act as stress concentration sites and crack propagation barriers, thereby limiting the overall length of delamination cracks. When *d* = 0.1257, the delamination crack length is reduced by 23.64%, and the delamination cracks are significantly suppressed. When *d* = 0.1885, the delamination crack length is reduced by 60.72%, and the crack morphology changes from planar propagation to a localized feature, confined only to the vicinity of the indenter contact zone. The above analysis results indicate that pore defects enhance the coating's resistance to delamination crack propagation.

To further quantitatively describe the relationship between the delamination crack length and pore density, the ratio of the delamination crack length *L* to the pore density *d* is defined as the pore density factor *Q*, and its expression is given by Eq. (10):

$$Q = \frac{L}{\mathrm{d}}$$

10

The variation of the pore density factor with pore density is shown in Fig. 6. Since *Q* exhibits a singularity (tending to infinity) as d approaches zero, the data point at *d* = 0 was excluded. When *d* = 0.0628 and *d* = 0.0943, the corresponding *Q* values are as high as 14457.17 and 9041.08, respectively. When *d* = 0.1257, the decrease in *Q* slows down to 5943.91. When *d* = 0.1571, the *Q* value further moderates, reaching 3961. When *d* = 0.1885, *Q* reaches 2038.83. The above analysis indicates that *Q* decreases as *d* increases, implying that the crack length per unit pore density decreases; that is, the inhibitory effect of increasing pore density on crack propagation is enhanced. This parameter provides a theoretical reference for the performance optimization of coatings.

As shown in Fig. 7, the stress distributions in the Y direction of the coating system are presented for pore densities of 0, 0.0943, and 0.1885, respectively.

From Fig. 7a, it can be seen that when d = 0, the stress distribution in the coating system is relatively continuous. The stress beneath the indenter transitions from dark blue to green, and the stress propagates to a relatively deep level, exhibiting a "bulb-shaped" pattern. This indicates that this region is the zone of maximum compressive stress concentration and is also the area most susceptible to material damage.

From Fig. 7b, it can be seen that when pore defects are present, stress concentration occurs around the pores, indicating that the pores bear part of the compressive load and thereby alleviate the stress concentration in the matrix. Compared with Fig. 7a, the compressive stress zone in Fig. 7b is more concentrated on the coating surface and the shallow layer beneath the indenter, and the "bulb-shaped" zone becomes narrower and shorter. This indicates that an appropriate amount of pores can effectively disperse and weaken local stress concentration, thereby enhancing the damage resistance of the coating.

From Fig. 7c, it can be seen that the blue-green region is extremely small, while most of the area is yellow to red, and the stress gradient is more gradual. This indicates that a higher pore density significantly reduces the stress concentration in the coating.

In summary, since the pores deform under compressive stress and cracks propagate simultaneously, this process releases energy. A higher pore density means that the coating can disperse and absorb more energy, resulting in a reduction in the area of the stress concentration zone within the coating.

4.2 Effect of Pore Shape on Delamination Cracks

The pore shapes within the coating are diverse, and differences in pore shape can exert varying influences on crack propagation. This subsection focuses on investigating the effect of pore shape on coating damage. Taking the pore density d = 0.1257 as an example, Fig. 8 show the crack propagation conditions in coating systems containing circular pores, square pores, and triangular pores under indentation loading. It can be seen from the figures that as the pore shape changes from circular to square and then to triangular, the corresponding delamination crack length gradually increases. This indicates that triangular pores cause the most severe damage to the coating, followed by square pores, while circular pores cause the least damage.

From the local magnified views of the pores, it can be seen that cracks around circular pores propagate in a relatively random manner, and cracks can initiate from various positions around the pore. In contrast, for square and triangular pores, cracks mainly propagate along the sharp corners of the pores. This is primarily because, under indentation loading, when stress concentration occurs around the pores, the stress concentration for triangular and square pores appears at the inner corners of the pores (the inner angle is 360° for a circular pore, 90° for a square pore, and 60° for a triangular pore). As the pore shape changes from circular to square and then to triangular, the inner angle gradually decreases. The smaller the inner angle, the more prone the pore is to stress concentration, which in turn makes crack initiation easier. This is consistent with the conclusions of Yang[25]. The above results indicate that the sharper the pore corners, the more severe the stress concentration and the longer the delamination cracks. Compared with pores having sharp corners, circular pores exhibit a stronger hindering effect on crack propagation.

As shown in Fig. 9, the stress distribution contour plots of coating systems with different pore shapes are presented. Limited by the measurement accuracy, it is difficult to display the stress concentration at

the sharp corners of the defects in the stress contour plots. However, the variation in the area of the compressive stress zone can indirectly reflect that, as the pore shape changes from circular to square and then to triangular, the area of the compressive stress zone (blue-green) gradually increases. This further indicates that circular pore defects have the greatest hindering effect on stress propagation within the coating system, followed by square pores, while triangular pores have the least hindering effect on stress propagation.

4.3 Mechanical Property Analysis

The testing and analysis of the system's mechanical properties help reveal the coating failure mechanism and predict the laws of crack initiation and propagation. Accurate mechanical parameters are a prerequisite for ensuring the accuracy of numerical simulations, and can also provide a basis for optimizing the coating material system and improving the preparation process, thereby enhancing the thermal shock resistance and service life of the coating.

In indentation test, the method proposed by Oliver and Pharr[26] is commonly adopted to evaluate the indentation hardness and indentation modulus during the unloading stage. First, the indenter is loaded at a certain loading rate until the load reaches its maximum value, and then unloaded at a certain unloading rate. Figure 10 shows the finally obtained load–displacement curve, which consists of two stages: loading and unloading. In the figure, h_{max} is the maximum indentation depth, and h_c is the contact depth, which can be determined from the intersection of the initial linear portion of the unloading curve with the horizontal axis.

The indentation hardness H_M is calculated using Eq. (11):

$$H_{\mathrm{M}} = \frac{P_{\max}}{A_{\mathrm{c}}} \quad (11)$$

Where $P_{\max}$ is the maximum load borne by the indenter, and A_c is the projected contact area between the tested material and the indenter, which is calculated using Eq. (12):

$$A_{\mathrm{c}} = 24.56{h_{\mathrm{c}}}^2 \quad (12)$$

Where h_c is the contact depth.

The indentation modulus can be obtained indirectly through the reduced modulus. The reduced modulus E_r is calculated using Eq. (13):

$$E_r = \frac{\sqrt{\pi}}{2\xi}\frac{S}{\sqrt{A_c}}$$

13

Where β is a geometric parameter of the indenter, which is 1.012 for a Vickers indenter, and S is the contact stiffness, which is calculated using Eq. (14):

$$S = \frac{dp}{dh}\Big|_{h\max} = \frac{P\max}{h\max - h_c} = \frac{P\max}{h\max(1 - h_c/h\max)} \quad (14)$$

Where, d_p and d_h are the load increment and indentation depth increment, respectively, within the range of 60%–95% of the maximum unloading load.

The relationship between the indentation modulus E_M of the coating and the reduced modulus E_r is given by Eq. (15):

$$\frac{1}{E_r} = \frac{1-\nu^2}{E_M} + \frac{1-{\nu_i}^2}{E_i}$$

15

Where E_i and v_i are the elastic modulus and Poisson's ratio of the indenter, respectively. In the discrete element method, the indenter is assumed to be a rigid body, therefore, E_i tends to infinity, and $1/E_i$ tends to zero. After simplification, Eq. (15) becomes Eq. (16):

$$\frac{1}{E_r} = \frac{1\text{-}\nu^2}{E_M} \quad (16)$$

For predicting the variation of indentation modulus of porous coatings with pore density under indentation loading, the Mori–Tanaka scheme (abbreviated as the M–T scheme)[27] can be adopted. It is a classical method for predicting the effective properties of multiphase materials and has been widely used in the mechanical property analysis of composite materials and porous materials, enabling the prediction of the equivalent elastic properties of composites. The prediction model expression for the normalized indentation modulus is given by Eq. (17)[28]:

$$E_M/E_{M0} = \frac{1-d}{1+2d} \quad (17)$$

Where d is the pore density, and E_{M0} is the indentation modulus corresponding to a coating pore density of 0.

The results predicted by the M–T scheme were compared with the numerical simulation results and the experimental results of Vanstreels[29], as shown in Fig. 11a. The simulation results are consistent with the trends of the M–T scheme predictions and the experimental results, that is, as the pore density increases, the indentation modulus of the porous coating exhibits a gradually decreasing trend. The numerical results were fitted using a nonlinear equation. The results indicate that pore shape also has a certain influence on the mechanical properties: circular pores have the least influence on the mechanical properties of the coating, while triangular pores have the greatest influence. This variation pattern is consistent with the influence of pore shape on delamination crack length discussed in Section 4.2,

further indicating that pores with smaller inner angles are more likely to weaken the mechanical properties of the coating.

Figure 11b shows the normalized indentation hardness results. The results indicate that its variation trend is similar to that of the indentation modulus. Both the normalized indentation modulus and indentation hardness decrease by approximately 50%, and both indicate that an increase in pore density reduces the mechanical properties of the coating system.

5. Conclusions

This paper investigated the damage to TBCs system caused by defects with different pore densities and pore shapes under indentation loading, and conducted a detailed analysis of crack propagation and mechanical properties of the coating. The conclusions are as follows:

(1) Under indentation loading, the damage to the coating system mainly occurs within the TC layer and at the TC/BC interface. Shear bands and coating delamination were observed in the numerical simulation. When the penetration depth of the indenter reaches 100 μm, cracks propagate downward from the surface of the TC layer and penetrate through the TC layer along the grain boundaries, eventually extending to the TC/BC interface. The simulation results are in good agreement with the experimental results, verifying the reliability of the model.

(2) With respect to pore density, a higher pore density can alleviate the stress concentration at the TC/BC interface and reduce the delamination crack propagation length. When the pore density increases from 0 to 0.1885, the delamination crack length is reduced by 60.72%. By defining the pore density factor Q, the negative correlation and attenuation characteristics between the delamination crack length and pore density were quantitatively described.

(3) With respect to pore shape, the degree of influence on coating damage follows the order: triangular pores > square pores > circular pores. The fundamental reason is that the smaller the inner angle of the pore, the more prone it is to stress concentration, thereby promoting crack initiation and propagation.

(4) The mechanical properties of TBCs gradually decrease with increasing pore density. Both the normalized indentation modulus and indentation hardness decrease with increasing pore density, and the numerical simulation results are consistent with the variation trends of the M–T theoretical model and experimental results, verifying the accuracy of the numerical simulation results.

In summary, this study established a discrete element numerical model and investigated the crack propagation behavior of the TBCs system under indentation loading. Through comparison between theoretical predictions and numerical simulation results, the reliability of the model was verified. This study can provide a theoretical basis for controlling pore density during coating processing. Although this paper mainly adopts the numerical simulation method and the model is a simplified two-

dimensional model, future work will carry out experiments based on this study to further verify the research conclusions.

Declarations

Conflict of interest:

On behalf of all authors, the corresponding author states that there is no conflict of interest.

Author Contribution

Hongfei Gao constructed the discrete-element numerical model and performed simulation analysis; Minglei Bai participated in data sorting and manuscript revision. All authors read and approved the final manuscript.

Acknowledgments:

This research did not receive any specific grant from funding agencies in the public, commercial, or not-for-profit sectors.

References

1. Liu, B., et al., Advances on strategies for searching for next generation thermal barrier coating materials. Journal of Materials Science & Technology, 2019. 35(5):833–851.
2. Kim, H., et al., Thermal barrier coating for carbon fiber-reinforced composite materials. Composites Part B: Engineering, 2021. 225:109308.
3. Viswanathan, V., G. Dwivedi, and S. Sampath, Multilayer, multimaterial thermal barrier coating systems: design, synthesis, and performance assessment. Journal of the American Ceramic Society, 2015. 98(6):1769–1777.
4. Cui, S., et al., Mechanical analysis and modeling of porous thermal barrier coatings. Applied Surface Science, 2020. 512:145706.
5. Qiao, X., et al., Influence of pores on mechanical properties of plasma sprayed coatings: Case study of YSZ thermal barrier coatings. Ceramics International, 2018. 44(17):21564–21577.
6. Hille, T.S., et al., Damage growth triggered by interface irregularities in thermal barrier coatings. Acta Materialia, 2009. 57(9):2624–2630.
7. Bumgardner, C., B. Croom, and X. Li, High-temperature delamination mechanisms of thermal barrier coatings: In-situ digital image correlation and finite element analyses. Acta Materialia, 2017. 128:54–63.

8. Wang, L., et al., Modeling of thermal properties and failure of thermal barrier coatings with the use of finite element methods: A review. Journal of the European Ceramic Society, 2016. 36(6):1313–1331.
9. Lawn, B.R., Indentation of ceramics with spheres: a century after Hertz. Journal of the American ceramic society, 1998. 81(8):1977–1994.
10. Rhee, Y.W., et al., Brittle fracture versus quasi plasticity in ceramics: a simple predictive index. Journal of the American Ceramic Society, 2001. 84(3):561–565.
11. Bäker, M., Finite element simulation of interface cracks in thermal barrier coatings. Computational Materials Science, 2012. 64:79–83.
12. Du, F., M.R. Lovell, and T.W. Wu, Boundary element method analysis of temperature fields in coated cutting tools. International Journal of Solids Structures, 2001. 38(26–27):4557–4570.
13. Ferguen, N., W. Leclerc, and E.-S. Lamini, Numerical investigation of thermal stresses induced interface delamination in plasma-sprayed thermal barrier coatings. Surface Coatings Technology, 2023. 461:129449.
14. Abdelgawad, A. and K. Al-Athel, Effect of TGO thickness, pores, and creep on the developed residual stresses in thermal barrier coatings under cyclic loading using SEM image-based finite element model. Ceramics International, 2021. 47(14):20064–20076.
15. Cundall, P.A. A computer model for simulating progressive, large-scale movements in blocky rock systems. in ISRM International Symposium. 1971.
16. Rackl, M. and K.J. Hanley, A methodical calibration procedure for discrete element models. Powder technology, 2017. 307:73–83.
17. Zhang, G., et al., Micro-and macrocracking behaviors in granite and molded gypsum containing a single flaw. Construction Building Materials, 2021. 292:123452.
18. Shimamura, K., et al., Thermophysical properties of rare-earth-stabilized zirconia and zirconate pyrochlores as surrogates for actinide-doped zirconia. International Journal of Thermophysics, 2007. 28(3):1074–1084.
19. Zhu, S.Z., et al., Influence of Adding ZrO2 on the Properties of La2Zr2O7 Ceramic. Key Engineering Materials, 2014. 602:335–339.
20. Zhang, J., et al., Modeling of machining process of EB-PVD ceramic coatings using discrete element method. CIRP Journal of Manufacturing Science &Technology, 2022. 38:581–589.
21. Renteria, A.F., et al., Application of USAXS analysis and non-interacting approximation to determine the influence of process parameters and ageing on the thermal conductivity of electron-beam physical vapor deposited thermal barrier coatings. Surface Coatings Technology, 2007. 201(8):4781–4788.
22. Yan, J., et al., On cracks and delaminations of thermal barrier coatings due to indentation testing: Experimental investigations. Acta materialia, 2008. 56(15):4080–4090.
23. Li, X., et al., Influence of random pore defects on failure mode and mechanical properties of SiC ceramics under uniaxial compression using discrete element method. Ceramics International, 2018.

44(18):22271–22282.
24. Wang, Y., et al., Effects of pore microstructure on the effective thermal conductivity of thermal barrier coatings. Applied Thermal Engineering, 2016. 102:234–242.
25. Yang, M., et al., Effect of five kinds of pores shape on thermal stress properties of thermal barrier coatings by finite element method. Ceramics International, 2017. 43(13):9664–9678.
26. Oliver, W.C. and G.M. Pharr, An improved technique for determining hardness and elastic modulus using load and displacement sensing indentation experiments. Journal of materials research, 1992. 7(6):1564–1583.
27. Benveniste, Y., On the Mori-Tanaka's method in cracked bodies. Mechanics Research Communications, 1986. 13(4):193–201.
28. Richter, H., Homogenisation of porous thin films and perforated layers: Comparison of analytical and numerical approaches. Mechanics of Materials, 2015. 89:119–129.
29. Vanstreels, K., et al., Effect of pore structure of nanometer scale porous films on the measured elastic modulus. Langmuir, 2013. 29(38):12025–12035.

Figures

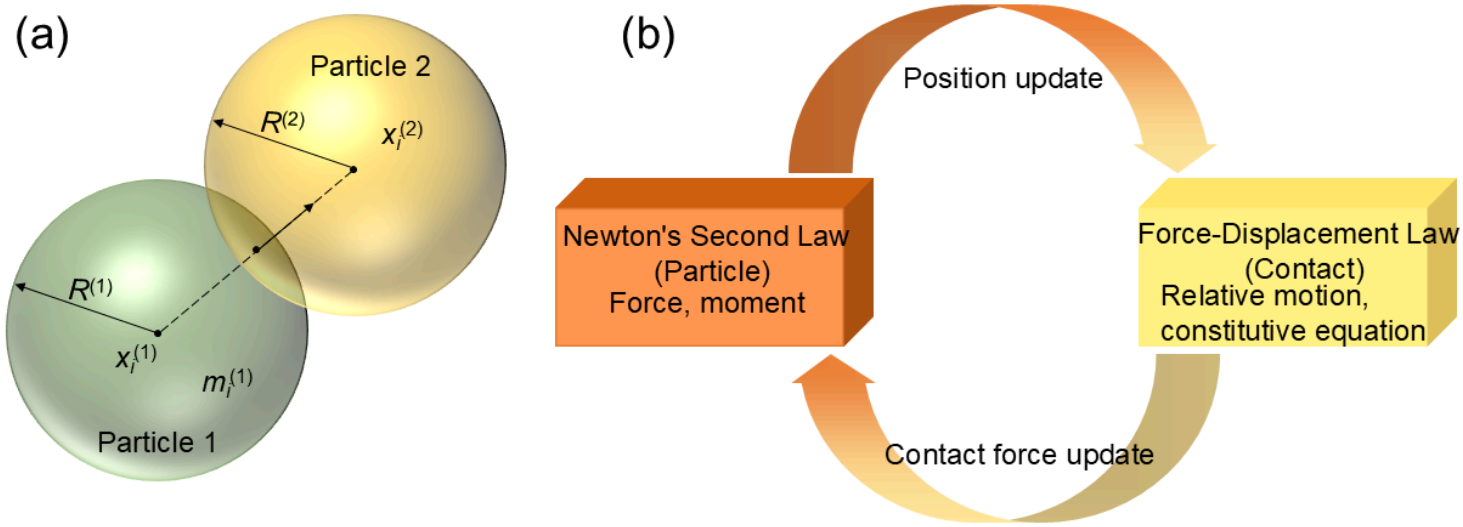


Figure 1

Particle contact model and iterative calculation cycle of DEM (a) Contact geometry of two particles (b) Calculation cycle of DEM.

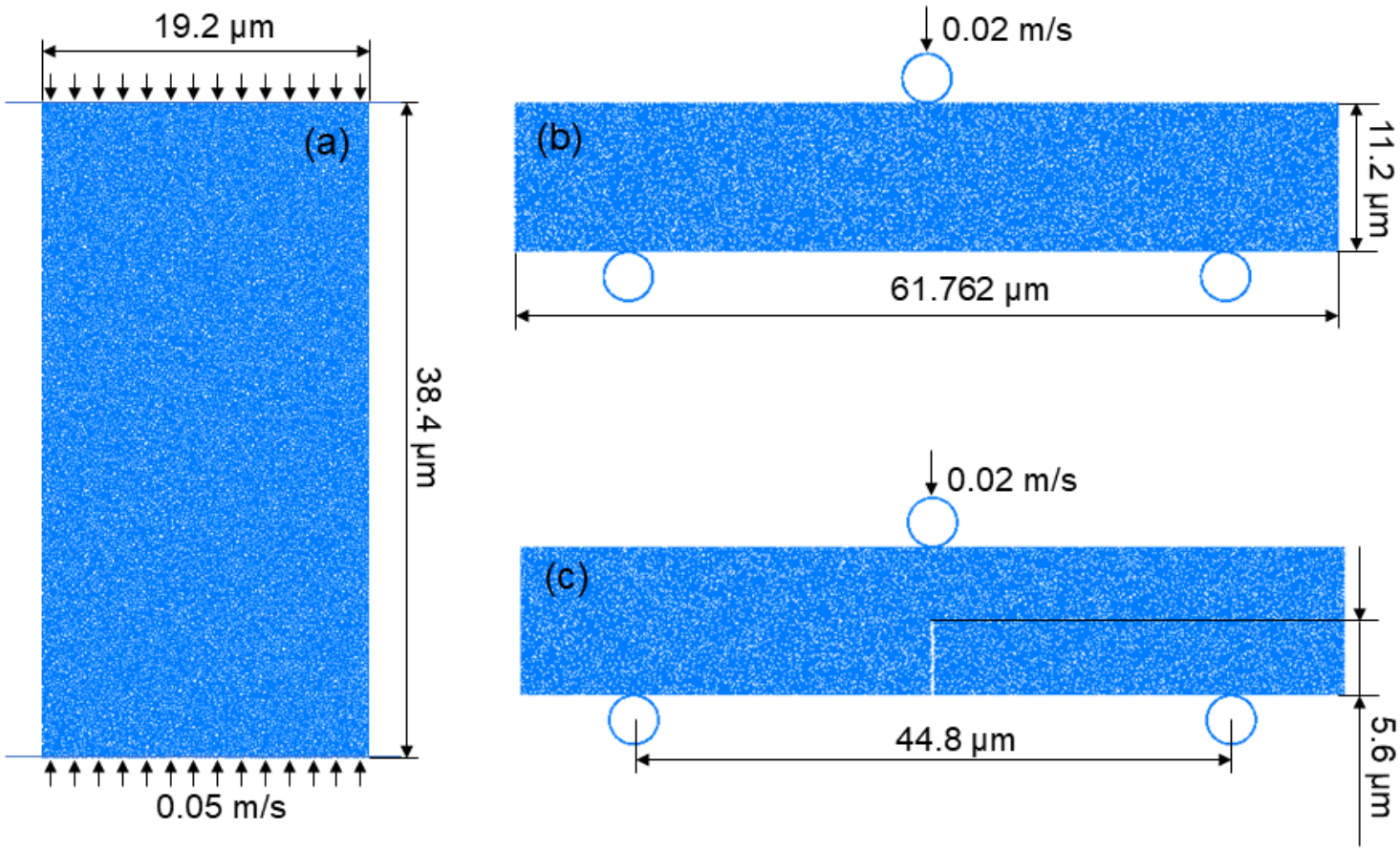


Figure 2

Parameters calibration experiment (a) Uniaxial compression test (b) Three-point bending test (c) Fracture toughness test

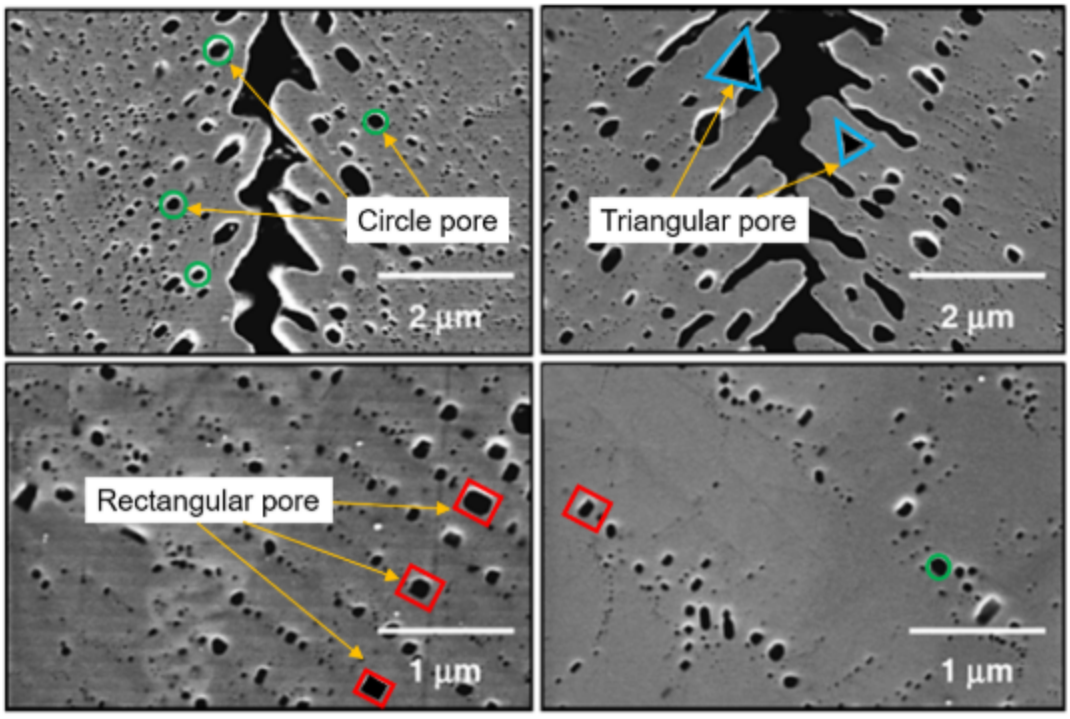


Figure 3

Microscopic SEM image of an EB-PVD coating containing random pores[21]

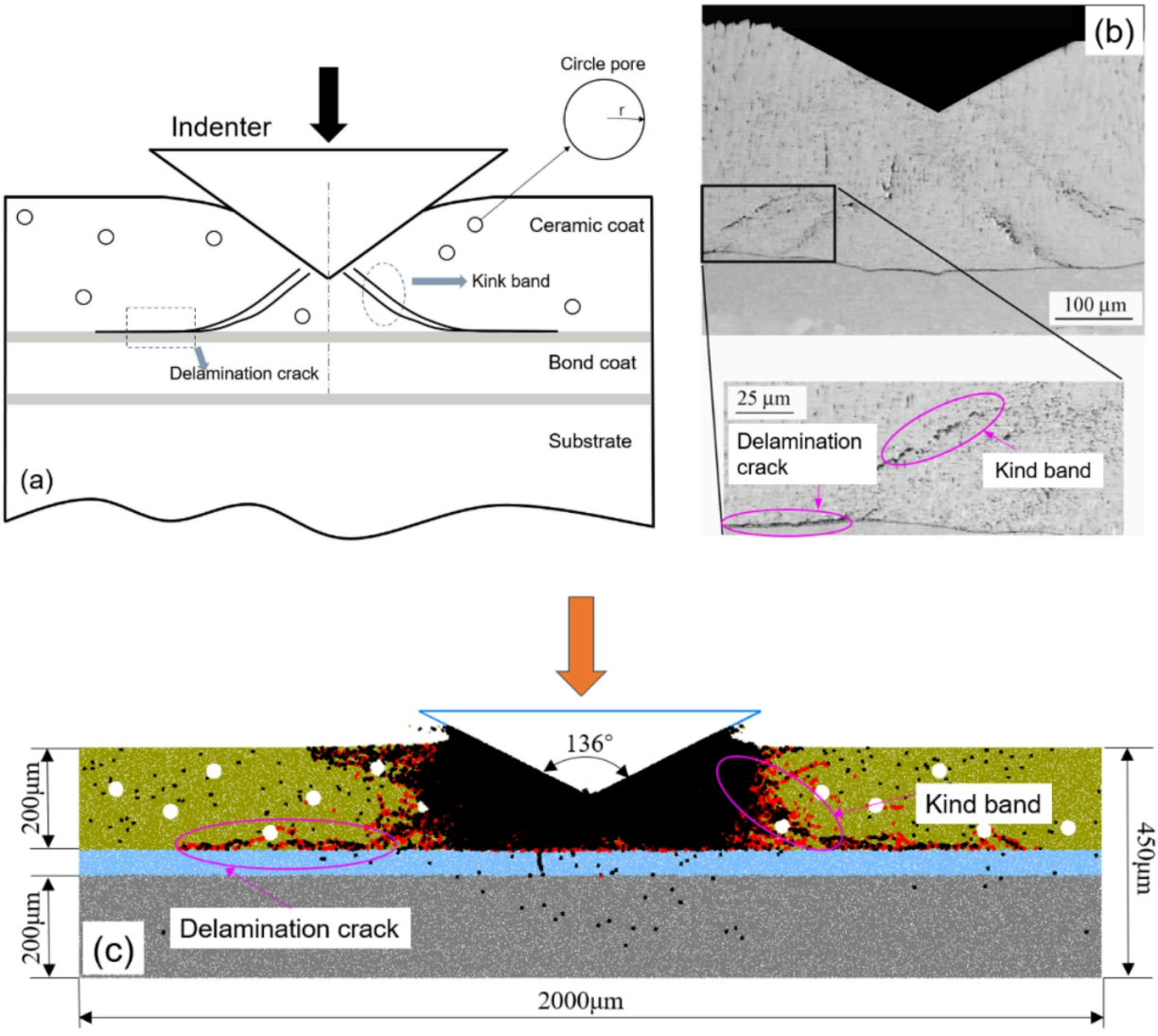


Figure 4

Delamination damage of the coating under indentation loading: (a) Theoretical model (b) Experimental results[22] (c) Discrete element numerical model

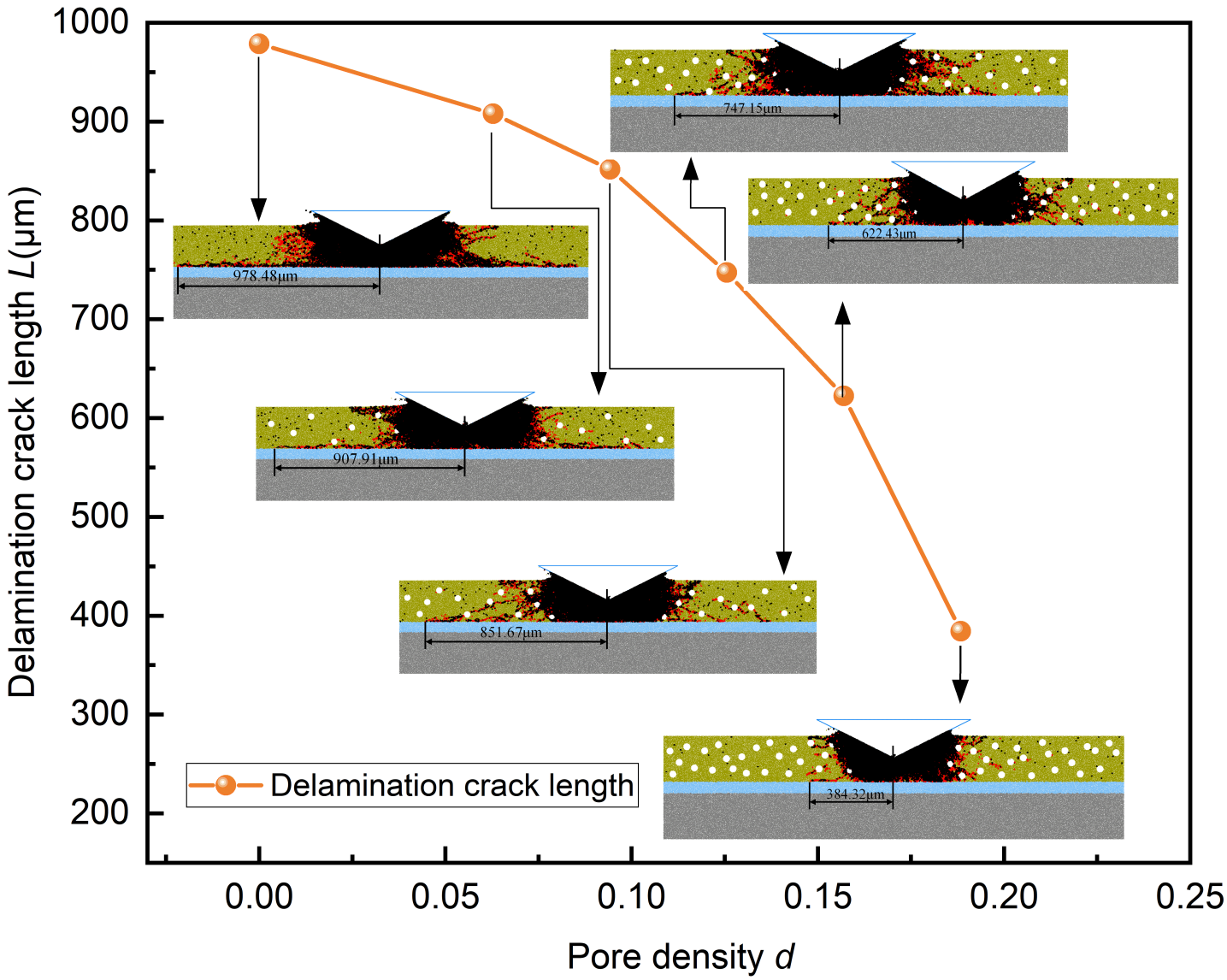


Figure 5

Variation trend of delamination crack length with pore density

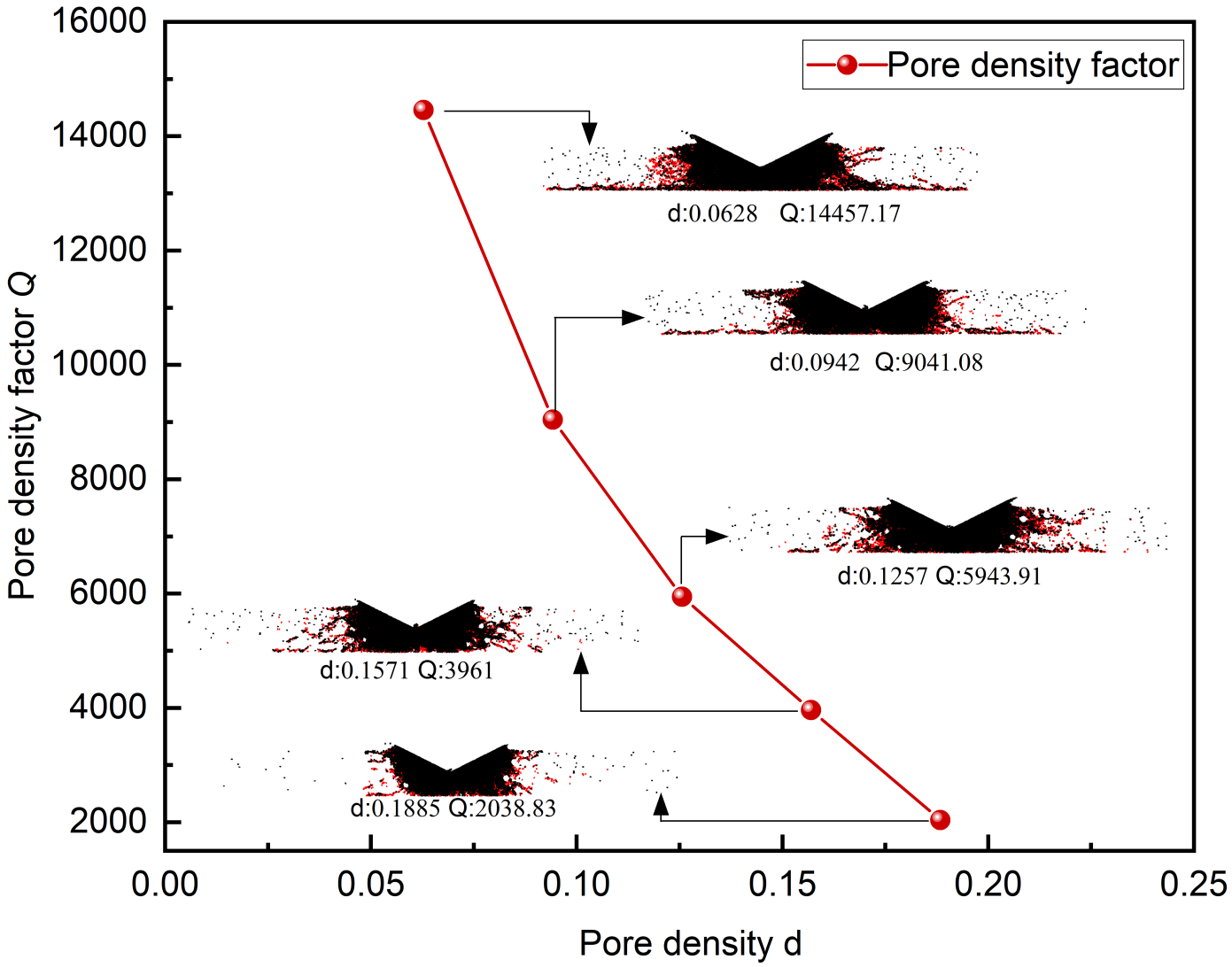


Figure 6

Variation trend of the pore density factor with pore density

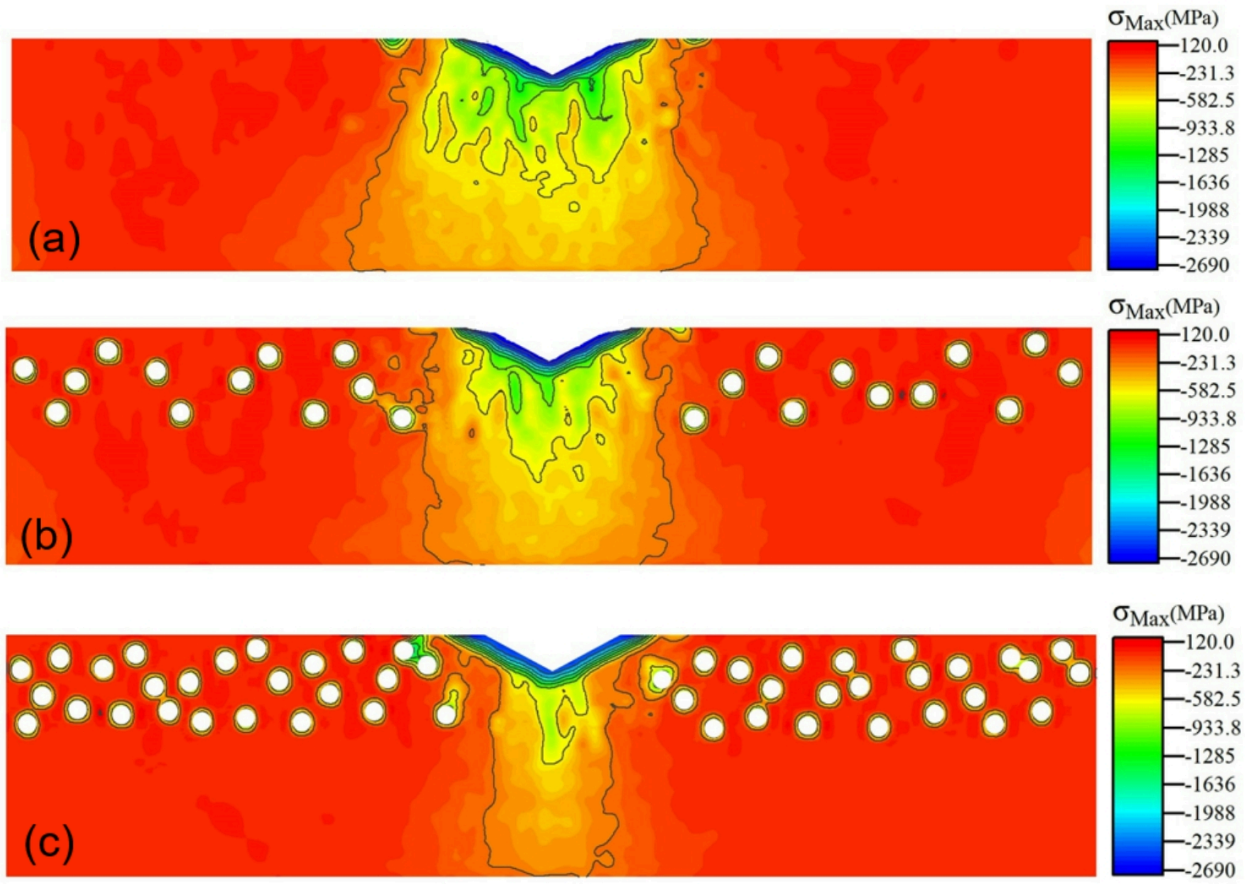


Figure 7

Stress distribution contour plots of coating systems with different pore densities (a) *d* = 0 (b) *d* = 0.0943 (c) *d* = 0.01885

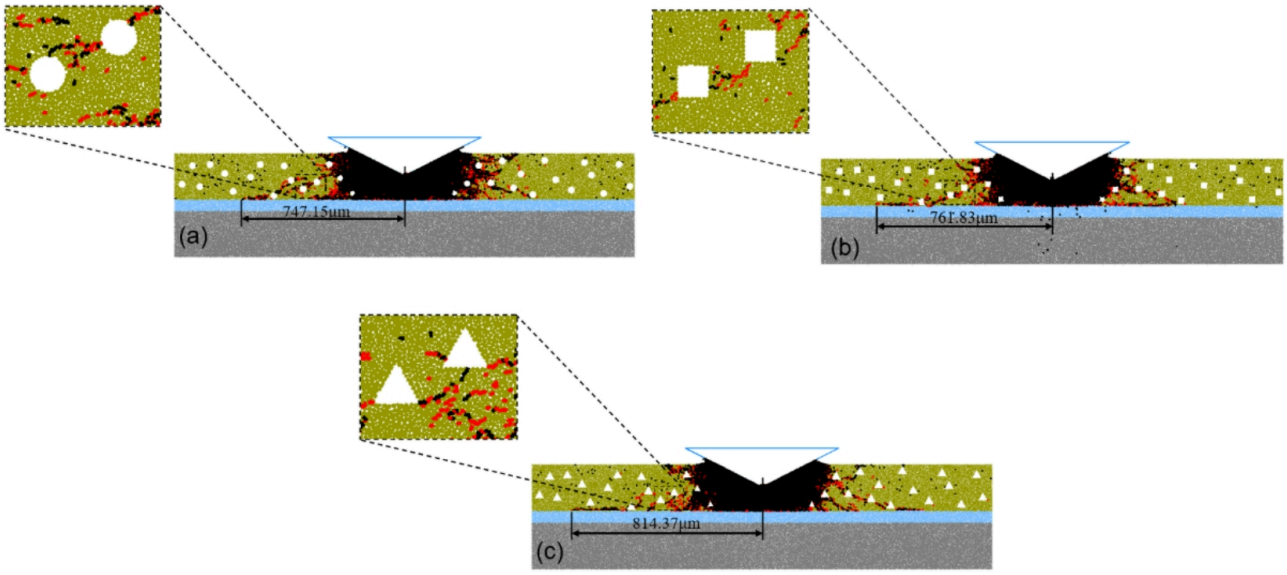


Figure 8

Effect of pore shape on delamination crack propagation: (a) Circular pore (b) Square pore (c) Triangular pore

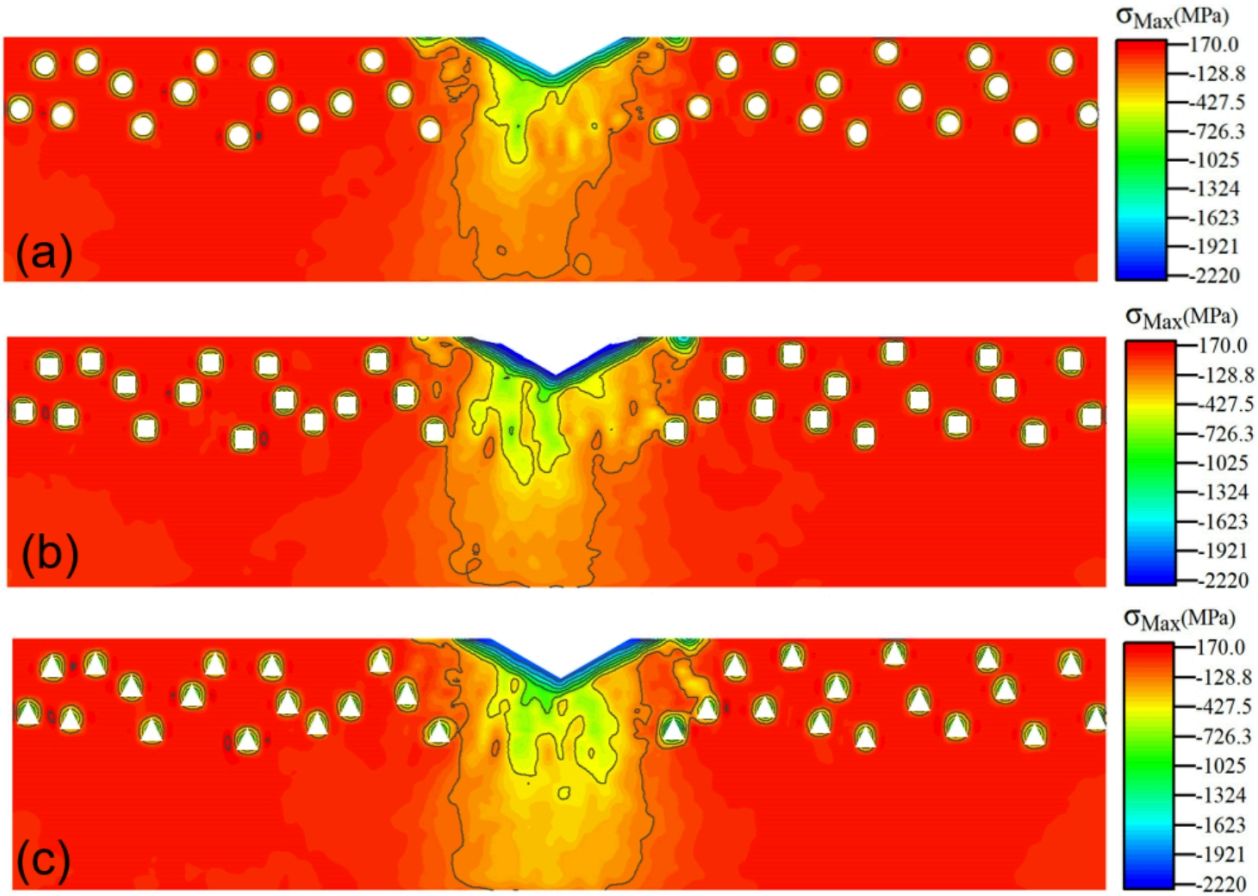


Figure 9

Stress distribution contour plots of coating systems with pore defects of different shapes: (a) Circular pore, (b) Square pore, (c) Triangular pore

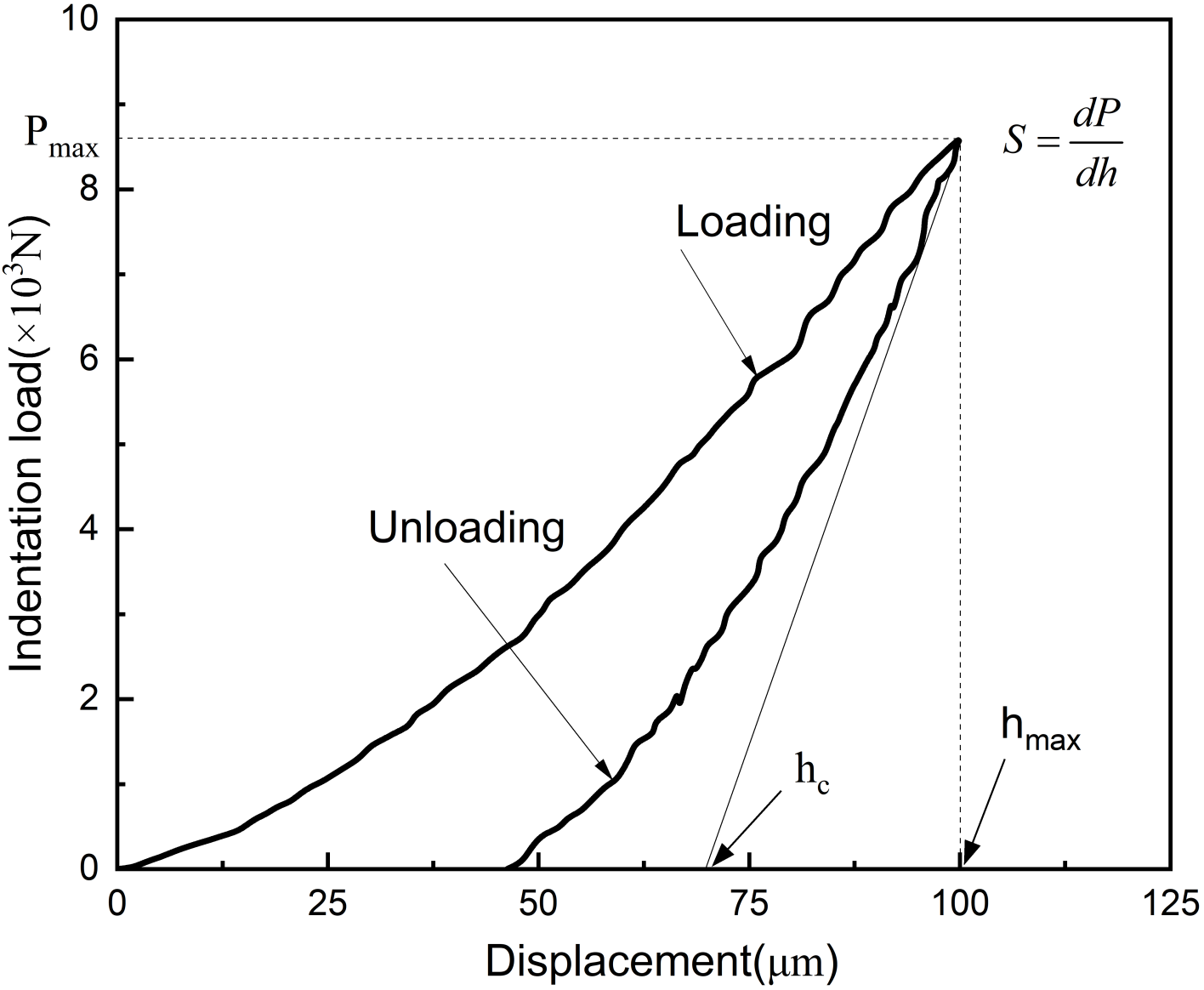


Figure 10

Indentation load–displacement curve of the indentation test

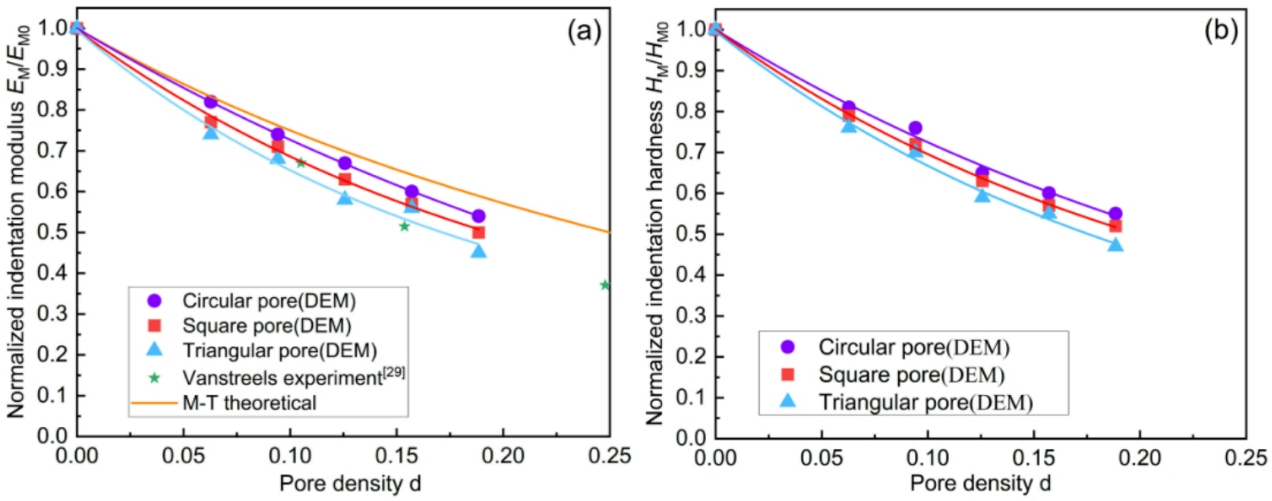


Figure 11

Variation of indentation modulus and indentation hardness with pore density: (a) Normalized indentation modulus (b) Normalized indentation hardness